Journal of Colloid and Interface Science 679 (2025) 487–495

Contents lists available at ScienceDirect

Journal of Colloid And Interface Science

journal homepage: www.elsevier.com/locate/jcis

Regular Article

Unveiling active sites in FeOOH nanorods@NiOOH nanosheets heterojunction for superior OER and HER electrocatalysis in water splitting

Sun Hua [a], Sayyar Ali Shah [a,d,*], Gabriel Engonga Obiang Nsang [a], Rani Sayyar [a,b], Badshah Ullah [a], Noor Ullah [a], Naseem Khan [a], Aihua Yuan [a,*], Abd. Rashid bin Mohd Yusoff [c], Habib Ullah [d,*]

[a] School of Environmental & Chemical Engineering, Jiangsu University of Science and Technology, Zhenjiang 212003, PR China
[b] School of Materials Science & Engineering, Jiangsu University of Science and Technology, Zhenjiang 212003, PR China
[c] Department of Physics, Faculty of Science, Universiti Teknologi Malaysia, Johor Bahru, Malaysia
[d] Department of Engineering, University of Exeter, Penryn Campus, Penryn, Cornwall TR10 9FE, United Kingdom

GRAPHICAL ABSTRACT

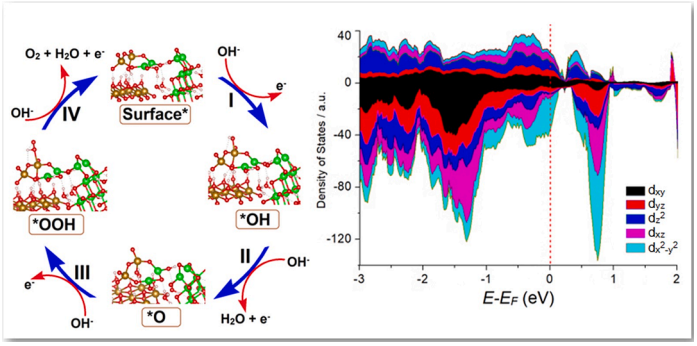

ARTICLE INFO

Keywords:
FeOOH nanorods@NiOOH nanosheets
Heterojunction
Overall water splitting
Electrocatalyst
Electronic properties

ABSTRACT

The development of cost-effective, highly active, and stable electrocatalysts for water splitting to produce green hydrogen is crucial for advancing clean and sustainable energy technologies. Herein, we present an innovative in-situ synthesis of FeOOH nanorods@NiOOH nanosheets on nickel foam (FeOOH@NiOOH/NF) at an unprecedentedly low temperature, resulting in a highly efficient electrocatalyst for overall water splitting. The optimized FeOOH@NiOOH/NF sample, evaluated through time-dependent studies, exhibits exceptional oxygen evolution reaction (OER) performance with a low overpotential of 261 mV at a current density of 20 mA cm^{-2}, alongside outstanding hydrogen evolution reaction (HER) activity with an overpotential of 150 mV at a current density of 10 mA cm^{-2}, demonstrating excellent stability in alkaline solution. The water-splitting device featuring FeOOH@NiOOH/NF-2 electrodes achieves a voltage of 1.59 V at a current density of 10 mA cm^{-2}, rivalling the state-of-the-art RuO_2/NF||PtC/NF electrode system. Density functional theory (DFT) calculations unveil the efficient functionality of the Fe sites within the FeOOH@NiOOH heterojunction as the active OER catalyst, while the Ni centres are identified as the active HER sites. The enhanced performance of OER and HER is

* Corresponding authors.
E-mail addresses: Sayyarali83@just.edu.cn (S.A. Shah), aihua.yuan@just.edu.cn (A. Yuan), hu203@exeter.ac.uk (H. Ullah).

https://doi.org/10.1016/j.jcis.2024.09.219
Received 16 September 2024; Accepted 27 September 2024
Available online 3 October 2024

attributed to the tailored electronic structure at the heterojunction, modified magnetic moments of active sites, and increased electron density in the dx^2-y^2 orbital of Fe. This work provides critical insights into the rational design of advanced electrocatalysts for efficient water splitting.

1. Introduction

In order to replace fossil fuel for hydrogen production in the future, water splitting is regarded as one of the promising, carbon–neutral, and facile approaches for obtaining clean and sustainable hydrogen fuel [1]. Overall water splitting proceeds through cathodic and anodic half-reaction i.e., hydrogen evolution reaction (HER) and oxygen evolution reaction (OER), respectively [1,2]. Generally, these half-reactions are relatively sluggish in kinetics especially the OER due to four proton-coupled electron transfer and a main issue of overall water splitting [3,4]. Therefore, a highly active catalyst is required to overcome the activation barrier and the sluggish reaction kinetics of overall water splitting. Pt-based materials are well-documented catalysts for HER and Ir- or Ru-based materials are known as efficient catalyst for OER [5,6]. However, these catalytic metals are costly and scarce, which limits their large-scale industrial applications [7]. It is essential to design and prepare inexpensive, earth-abundant, and equally effective electrocatalyst for both OER and HER.

Several efforts have been devoted in developing precious metal-free electrocatalyst for overall water splitting with good performance and stability. In this regard, 3d Metal oxyhydroxide-based electrocatalysts have attracted great interest for water splitting performance [8–10]. For example, Iron (oxy)hydroxide (FeOOH) has been successively explored for electrocatalytic water splitting performance and stability [11–15]. However, single 3d metal (oxy)hydroxides still suffer from large overpotential and cannot achieve the desired results [16]. Recently, 3d metal (oxy)hydroxides nanocomposites were reported for enhanced electrocatalytic performance [17,18]. Wu *et. al.* electrochemically converted NiFe nitride and phosphide nanosheet arrays to NiOOH/FeOOH heterostructure composites on Ni foam (NF) and found outstanding OER performance with an overpotential of 292 mV to reach the current density of 500 mA cm^{-2} [19]. On the other hand, Wan and co-workers synthesized an urchin-like FeOOH@NiOOH heterostructure on NF and found excellent electrocatalytic activity for both OER and HER. The excellent activity can be attributed to the unique urchin-like morphology and the synergy between Ni and Fe species [20]. Wang *et al.* reported FeOOH nanosheet arrays and in-situ-generated NiOOH during an electrochemically cyclic process and produced FeOOH/NiOOH heterostructure for enhanced water splitting performance [21]. These results reveal that the syngenetic effect between Fe and Ni (oxy) hydroxides enhances the electrocatalytic performance.

Alternatively, precipitation or electrodeposition strategies are usually used for the synthesis of Fe and Ni oxyhydroxide materials [22–24]. The co-precipitation technique is frequently carried out in mild basic conditions and is difficult to control the morphology of products usually stack on top of each other [25]. In homogeneous hydrothermal or solvothermal precipitation, Fe and Ni layered double hydroxide are formed [26,27]. While electrocatalysts can be obtained through these methods, they are relatively time-consuming. Fe and Ni oxyhydroxides prepared via electrodeposition procedures are relatively facile and cost-effective [28,29]. However, the electrodeposition bath solution tends to be in the acid range. Synthesizing Fe and Ni oxyhydroxide electrocatalysts for water splitting performance through the hydrolysis route at low temperatures without the addition of surfactants or organic ligands is rarely reported.

In this study, we have presented a novel approach for synthesis of FeOOH nanorods decorated with NiOOH nanosheets on NF substrate, denoted as FeOOH@NiOOH/NF-X (where X represents the reaction time), via a low-temperature hydrolysis method. We found that the reaction time significantly influences the electrocatalytic performance of the material. The optimized FeOOH@NiOOH/NF-2 sample demonstrates excellent electrocatalytic activity for both OER and HER in 1 M KOH solution. Moreover, electrolysis using FeOOH@NiOOH/NF-2 as both the anode and cathode exhibits water splitting performance comparable to that of Pt/C and RuO electrodes. Through DFT simulations, we identified Fe and Ni are active sites for OER and HER within the FeOOH@NiOOH heterojunction, respectively. Additionally, the simulated electronic properties reveal a transformation in charge distribution within the heterojunction, shedding light on its underlying catalytic mechanisms.

2. Materials and methods

2.1. Synthesis of FeOOH@NiOOH/NF

The NF pieces with dimension into 3 × 1 cm kept in HNO_3 (M) solution for 30 min in the order to remove the surface oxides. It was washed with water and ethanol and then dried in vacuum oven for 6 h. The 0.2 g of each $FeCl_2$ and $NiCl_2$ were dissolved together in the 30 mL of water. Ni foam was carefully suspended in solution and kept in oil bath. The solution was vigorously magnetic stirred at 40 °C for 2 h. NF was removed and washed with water an ethanol four times and dried in vacuum oven. Similarly, other samples were prepared with same procedure and keeping experiment for 1, 3, and 4 h in oil bath (Table S1).

2.2. Synthesis of FeOOH/NF and NiOOH/NF

The same procedure and conditions were adopted for synthesis of FeOOH nanorods using 0.2 g of $FeCl_2$, while 0. 2 $NiCl_2$ solution was used for the synthesis of NiOOH nanosheets.

2.3. Characterizations

The microstructure and morphology of the samples were observed by SEM and TEM. The elementally mapping images were recorded by EDX attached TEM. Crystal phase structure of the as-prepared material was characterized by using X-ray diffraction (XRD). The Raman spectrum was recorded at wavelength by laser Raman spectrometer at room temperature. The surface composition and chemical valence state of the element in composite material was examined by X-ray photoelectron microscopy (XPS) using Thermo ESCALAB 250 XI spectrometer (Thermo Fisher Corporation).

2.4. Electrochemical measurements

All the as-prepared samples were tested for electrochemical performance using three-electrode electrochemical workstation system (CHI 760D, Shanghai, Chenhua Co. LTD). The as-prepared electrode without any binding was directly as a working electrode. The graphite rod (7 mm in diameter) and Hg/HgO electrode were selected as counter and reference electrodes, respectively. First, cyclic voltammetry (CV) scanning was tested at the scan rate of 100 mV/s for 100 cycles in alkaline solution of 1 M KOH. Then linear sweep voltammetry (LSV) measured at the scan rate of 5 mV/s in the same alkaline solution. CV cycles stability was measured at a scan rate of 100 mV/s in potential windows and V (vs. Hg/HgO) for HER and OER, respectively. The LSV curves was again measured after 1000–3000 CV cycles for both HER and OER. The amperometry (i-t) tests were measured at a constant potential for OER and HER for 24 h. The double-layer capacitance was calculated from CV curves at different scan rates of 5 mV/s in potential range of 0–0.1 V (vs.

Hg/HgO in order to investigate of electrochemical active surface area. Electrochemical impedance spectroscopy (EIS) measurements were tested in a frequency range from 100 kHz to 100 mHz by applying an AC voltage with 5 mV amplitude in 1 M KOH solution. The i-*t* test was performed for 100 h at current density 50 mA cm^{-2} to checked stability of sample. The catalytic electrodes used directly as anode and cathode for overall water splitting. Pt/C or RuO and Nafion solution were dispersed in water to prepared Pt/C or RuO inks. The Pt/C or RuO electrodes were constructed by depositing the Pt/C and RuO inks on NP.

2.5. Computational methodology

We utilized QuantumATK software for our simulations employing the Density Functional Theory (DFT) method with the Generalized Gradient Approximation (GGA) and Perdew-Burke-Ernzerhof (PBE) exchange–correlation functional. The NiOOH unit cell, based on Kazimirov et al.'s work [30], had a Trigonal crystal system and *P*3*m*1 space group, with lattice parameters of a = b = 2.98 Å, c = 4.58 Å, α = β = 90°, and γ = 120°. The FeOOH unit cell, also Trigonal with a *P*3*m*1 space group, had lattice parameters of a = 10.95 Å, b = 3.08 Å, c = 5.32 Å, α = γ = 90°, and β = 118.86°. After fully relaxing the unit cell of NiOOH and FeOOH, followed by replicating them, resulting in 64-atom structures (supercells), we optimized and cleaved them along the (1 0 0) direction for surface reactions like OER and HER. The final heterojunction catalyst is created from the equal contribution of NiOOH and FeOOH (NiOOH@FeOOH) along 100 directions and exposed for surface reactions (Details in Text of Supporting information).

3. Results and discussion

3.1. Synthesis and characterization

The synthesis process of FeOOH@NiOOH hybrid on the NF shown in Fig. 1a. The Fe and Ni ions solution under vigorous magnetic stirring hydrolyzed to form a FeOOH@NiOOH hybrid in NF substrate. The major product of direct hydrolysis is FeOOH phases confirmed in several reports [31,32]. The phase stability of different Fe^{3+} polymorphs including oxides/oxyhydroxides/hydroxides, depends on their sizes, surface energetics, and environment. The most stable phase in bulk is Fe_2O_3, while the presence of a hydrated environment at the nanoscale, FeOOH is predicted to be the most stable phase due to its much lower surface energy [33]. Furthermore, the hydrolysis of Fe^{3+} ions more favorable [Ksp for $Fe(OH)_3 = 4 \times 10^{-38}$] then Fe^{2+} [Ksp for $Fe(OH)_2$ is 8×10^{-16}] [34]. This suggests that Fe^{2+} ions do not significantly hydrolyze and precipitate. However, the Fe^{2+} ions can be easily oxides to Fe^{3+} with dissolved oxygen in water.

$$4Fe^{2+} + O_2 + 4H^+ \rightarrow 4Fe^{3+} + 2H_2O$$

This is followed by a hydrolysis reaction of Fe^{3+} to produce FeOOH.

$$Fe^{3+} + 2H_2O \rightarrow FeOOH + 3H^+$$

On the other hand, Ni^{2+} ions also undergo hydrolysis to generate NiOOH nanosheets during the synthesis process under similar conditions. The solubility product constant (Ksp) for $Ni(OH)_2$ is

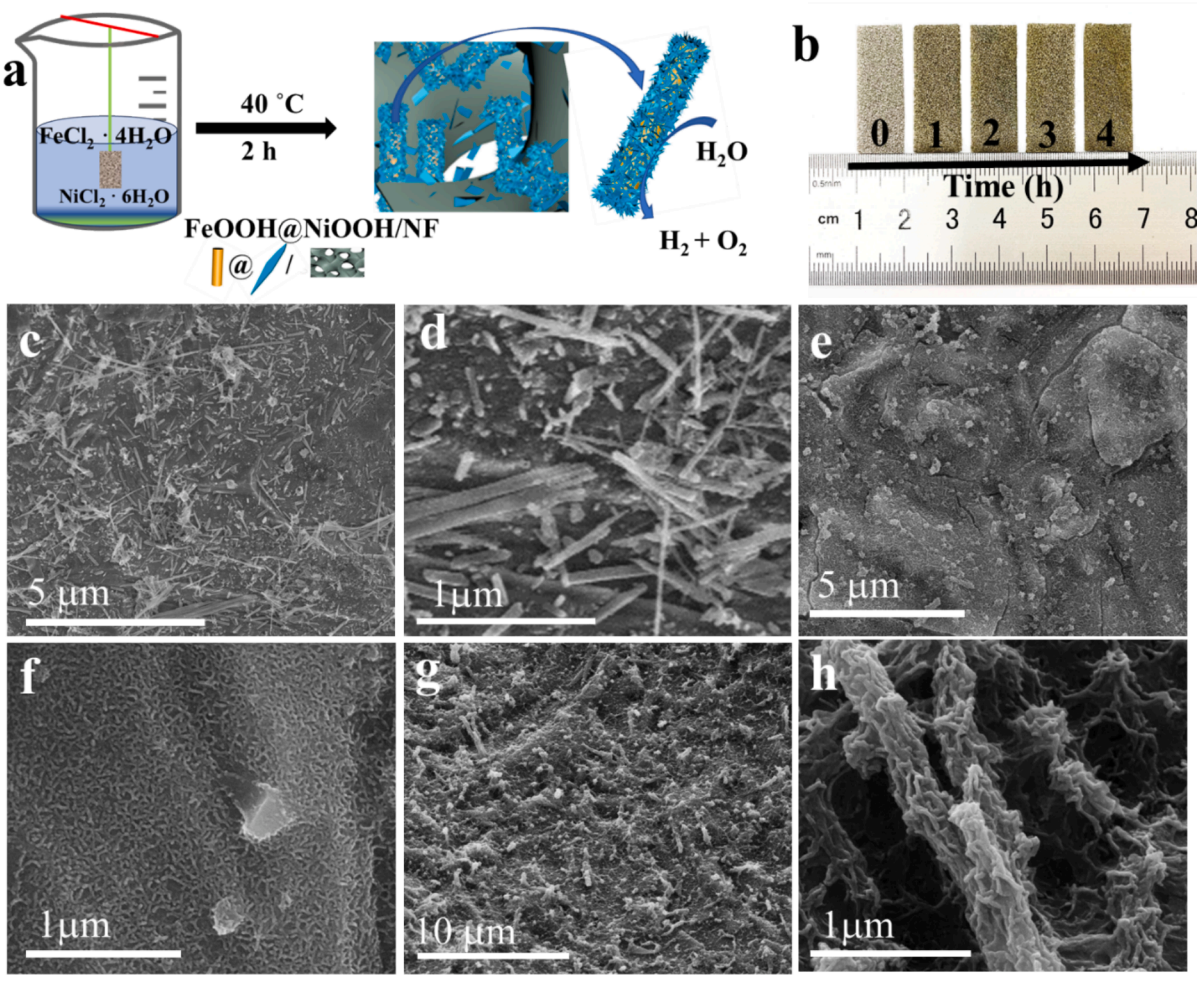

Fig. 1. A) Schematic illustration of the synthetic process of FeOOH@NiOOH/NF. **b)** Digital photographs of FeOOH@NiOOH catalyst loaded NF at various time intervals alongside bare NF. SEM images of **c, d)** FeOOH/NF-2, **e, f)** NiOOH/NF-2 and **g, h)** FeOOH@NiOOH/NF-2 samples.

approximately 2.0 × 10^{-15}, which means Ni^{2+} ions can stay in solution at near-neutral pH without substantial precipitation and allow it for gradual precipitation of $Ni(OH)_2$, which further oxidized to NiOOH nanosheets.

Since FeOOH forms more readily and rapidly under the conditions because Fe^{2+} is easily oxidated to Fe^{3+} than Ni^{2+} to Ni^{3+}, it is likely to be first precipitated. The FeOOH grow in nanorod morphology due to crystallographic twinning according to Mackay's Twin [35]. The slower formation and subsequent oxidation of $Ni(OH)_2$ to NiOOH may result in the NiOOH nanosheet phase being deposited around the FeOOH nanorods, leading to a core–shell-like structure. Shanmugapriya et al. also reported a one-pot synthesis of $Ni(OH)_2$NiOOH nanosheets/FeOOH nanorods heterostructure using a hydrothermal method [36]. Throughout the synthesis, the colour of the NF substrate changes from its original state to light brown initially and eventually to brown with time (refer to Table S1. Supporting Information and the digital photograph in Fig. 1b). For further insights into the synthesis process, please refer to the Experimental Section provided in the Supporting Information.

Fig. 1(c–h) presents scanning electron microscopy (SEM) images of our synthesized products. In Fig. 1c, the SEM image of the FeOOH/NF-2 sample reveals the presence of nanorods on the NF skeleton. These nanorods exhibit a nearly homogeneous distribution with lengths reaching up to several micrometres, as depicted in Fig. 1d. Additionally, a minimal number of nanoparticle-like structures can be observed on the NF surface. The surfaces of the nanorods appear relatively smooth and regular. Upon utilizing Ni salt as the initial precursor in the reaction, the NiOOH nanosheets grow on the NF skeleton. These NiOOH nanosheets exhibit a hierarchical-like morphology, predominantly growing vertically on the surfaces of the NF, as illustrated in Fig. 1e and f. A few flake-like structures can also be observed within this vertical corrugation morphology, possibly representing NiOOH nanosheets detached from the surface of the NF.

In the case of FeOOH@NiOOH hybrid samples, both Ni and Fe precursors were employed under the similar conditions. Fig. 1g and h demonstrate the presence of one-dimensional nanomaterials with corrugation morphology, where some nanosheets are also evident on the NF. Notably, these one-dimensional nanomaterials with corrugation morphology correspond to NiOOH nanosheets, grown on FeOOH nanorods. These nanosheets are extremely thin and nearly perpendicular to the nanorods.

The morphology and microstructure of FeOOH@NiOOH-2 composite were further elucidated through TEM observations. Fig. 2**a** illustrates a TEM image revealing the corrugation structure of the prepared sample. This structure presents a core–shell architecture revealed by a relatively dense black core surrounded by a transparent shell (Fig. 2b). The core consists of one-dimensional nanorods, while the shell exhibits a nanosheet morphology, with the transparency indicating the thin nature of the nanosheets, consistent with SEM observations. Furthermore, high-resolution TEM (HRTEM) analysis of the FeOOH@NiOOH composite is also performed as depicted in Fig. 2c. The lattice fringe with a spacing of 0.334 nm corresponds to the (130) plane of FeOOH, while the fringe

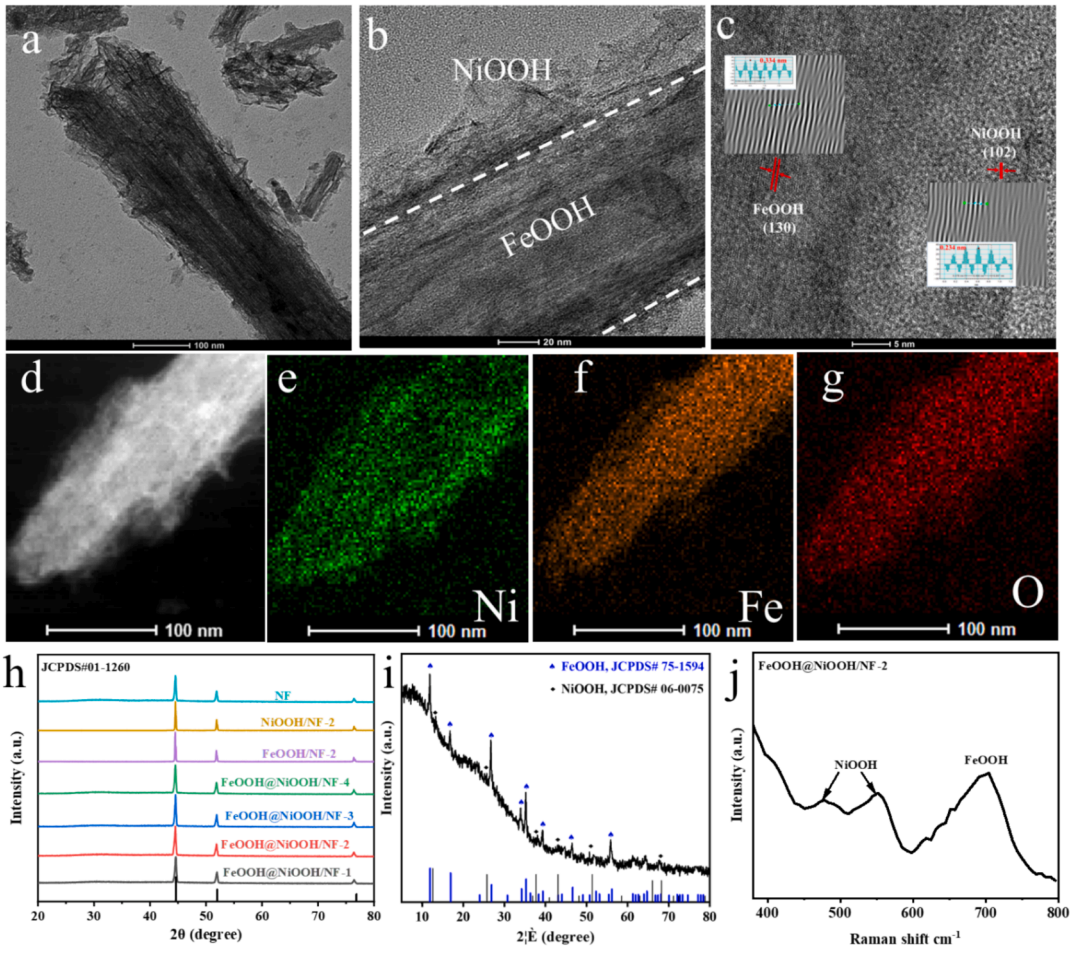

Fig. 2. a, b) TEM images showing the morphology of FeOOH@NiOOH/NF-2 composite. c) HRTEM image revealing detailed crystal structure. Inset image of Figure c shows the enhanced lattice fringes for $(102)_{NiOOH}$ and $(130)_{FeOOH}$ planes. d) Dark-field TEM image for enhanced contrast. Elemental mapping images displaying distribution of e) Fe, f) Ni, and g) O across the composite material. h) XRD patterns of the synthesized samples. i) XRD patterns of FeOOH@NiOOH collected from the surface of NF. j) Raman spectrum of the FeOOH@NiOOH/NF-2 composite.

spacing of 0.234 nm aligns with the (102) plane of NiOOH, confirming the composition of the product.

To assess the composition of the FeOOH@NiOOH hybrid, energy-dispersive X-ray spectroscopy (EDS) elemental mapping was conducted as shown in Fig. 2d–g. The intensity of the Ni signal appears higher at the edges in the elemental mapping image (Fig. 2e), whereas Fe is more concentrated at the centre of the FeOOH@NiOOH composite (Fig. 2f). Additionally, oxygen signals are uniformly distributed throughout the corrugation structure (Fig. 2g). These findings provide further evidence that NiOOH nanosheets grow on FeOOH nanorods, forming a nanorod-nanosheet FeOOH@NiOOH structure.

X-ray diffraction (XRD) analysis was employed to investigate the crystal phases present in the synthesized samples. The XRD patterns of the samples exhibited similar characteristics, displaying peaks at approximately 8.9°, 32.5°, and 56.8°, corresponding to the (002), (100), and (110) crystal phases of Ni (JCPDS No. 01-1260), respectively (Fig. 2h). However, other phase diffraction peaks were not observed in any of the samples, possibly due to their relatively low diffraction intensities. The diffraction peaks, centered at 11.9°, 16.8°, 26.8°, 34.1°, 35.2°, 39.4°, 46.6°, 52.3°, 56.1°, and 64.7°, correspond well with the crystal planes (110), (200), (130), (400), (211), (301), (411), (600), (251), and (541) of FeOOH phase (JCPDS No. 75–1594). The relative low intensity peaks at 12.9°, 26°, 37.9°, 43.3°, 51.6° are associated with (033), (006), (102), (105) (108) crystallographic planes of NiOOH (JCPDS No. 06–0075). The XRD patterns suggests that FeOOH and NiOOH phase exists in the product and NiOOH and FeOOH are successfully prepared. XRD results are consistent with HRTEM observations. Furthermore, the Raman spectrum is recorded for FeOOH@NiOOH/NF-2 sample (Fig. 2j). The peaks at 477 and 551 cm^{-1} are characteristic bands to the NiOOH nanosheets and peak centered at 698 cm^{-1} should be assigned to FeOOH phase of nanocomposite [19].

XPS analysis was performed to elucidate the surface chemical compositions and valence states of FeOOH/NF-2, NiOOH/NF-2, and FeOOH@NiOOH/NF-2 samples. The survey XPS spectra confirmed the presence of Fe, Ni, and O elements in all samples (Fig. S1a, Supporting Information). The Ni signal observed in the FeOOH/NF-2 sample originates from the NF surface. In the Ni 2p region of the FeOOH@NiOOH/NF-2 product, two spin–orbit doublet peaks appeared at 856.6 and 874.4 eV for Ni $2p_{3/2}$ and Ni $2p_{1/2}$ bands, respectively, indicative of Ni^{3+} oxidation state (Fig. S1b, Supporting Information) [31,37]. Additionally, satellite peaks at 862.4 and 880.5 eV were observed corresponding to the Ni $2p_{3/2}$ and Ni $2p_{1/2}$ bands, respectively [31]. The Fe $2p_{3/2}$ and Fe $2p_{1/2}$ binding energies of the FeOOH/NiOOH-2 sample were centered at 713.7 and 725.8 eV, respectively, consistent with the high valence state of Fe^{3+} (Fig. S1c, Supporting Information) [38,39]. Satellite peaks at 719.8 and 730.2 eV were also detected, indicating the presence of satellite bands for Fe $2p_{3/2}$ and Fe $2p_{1/2}$, respectively. Notably, in the FeOOH@NiOOH/NF-2 sample, the Fe $2p_{3/2}$ peak shifted to a lower binding energy of 713.4 eV compared to FeOOH/NF-2, suggesting an interaction between FeOOH nanorods and NiOOH nanosheets in the heterostructure composite. The O 1 s spectrum is deconvoluted into three components at binding energy 529.7, 531.6 eV, and 532.7 eV corresponding to O_2^{2-} and/or O^- and hydroxyl group (–OH), and absorbed oxygen or water molecules respectively (Fig. S1d, Supporting Information) [40]. The weak peak at 529.7 eV may be due to Ni and/or Fe oxide, while stronger peaks at 531.6 eV represent the bonding of Ni and Fe with hydroxyl group.

3.2. Electrochemical performance

The electrochemical performance of all catalysts was assessed in a 1 M KOH solution, with the linear sweep voltammetry (LSV) results for the oxygen evolution reaction (OER) depicted in Fig. 3**a**. Among the samples, FeOOH@NiOOH/NF-2 demonstrated the most favorable catalytic OER performance, exhibiting the lowest overpotential of 261 mV at a current density of 20 mA cm^{-2}. Notably, FeOOH@NiOOH/NF-1, FeOOH@NiOOH/NF-3, and FeOOH@NiOOH/NF-4 composites also

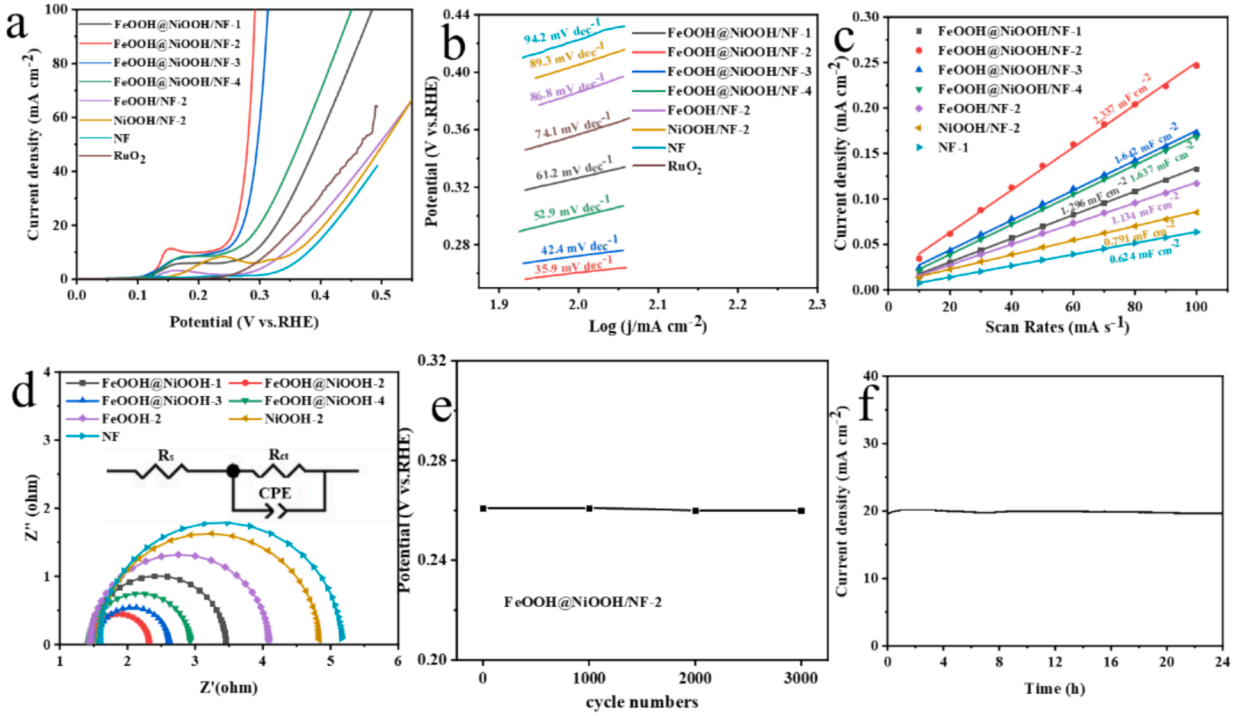

Fig. 3. A) the lsv curves of RuO catalysts and as-prepared samples, b) Tafel plots derived from LSV curves. c) The *Cdl* values was calculated by plotting the $\Delta J = (Ja-Jc)$ at 0.05 V vs. Hg/HgO against various scan rates in nonperiodic region. d) Nyquist plots and equivalent circuit (inset of d). e) Overpotential (V vs RHE) at constant current density 20 mA cm^{-2} of FeOOH@NiOOH/NF-2 composite before and after 1000–3000 CV cycles and f) the chronoamperometric curve of FeOOH@NiOOH/NF-2 composite.

displayed superior OER performance compared to the commercial RuO_2 catalyst (Table S2, Supporting Information). The relatively inferior OER performance of the FeOOH@NiOOH/NF-1 sample may be attributed to the lower amount of catalyst loaded on NF due to a shorter reaction time. Conversely, the FeOOH@NiOOH/NF-4 samples, with a reaction time of 4 h for catalyst loading, exhibited a high amount of catalyst growth on NF, potentially blocking most active sites for OER performance. It is suggested that an optimal reaction time of approximately 2 h for loading the catalyst on NF yields the best OER performance, with FeOOH@NiOOH/NF-2 demonstrating superior or comparable OER performance to other reported Fe and Ni-based oxyhydroxide materials. The overpotentials of NiOOH/NF-2 and FeOOH/NF-2 catalysts were 406 mV and 387 mV, respectively, at a current density of 20 mA cm^{-2}, indicating poor OER performance of the as-prepared samples. Ni foam exhibited the worst OER performance, with an overpotential of only 421 mV at a current density of 10 mA cm^{-2}. FeOOH@NiOOH/NF-2 catalyst displayed comparable or superior performance to previously reported FeOOH and/or NiOOH-based catalysts in alkaline solutions (Table S3, Supporting Information). The enhanced OER performance of FeOOH@NiOOH/NF-2 composite nanomaterials can be attributed to the synergistic effect between FeOOH nanorods and NiOOH nanosheets, with NF serving as a growth substrate for the catalysts and providing a conductive substrate. Additionally, analysis of the Tafel plots revealed a smaller Tafel slope of 35.9 mV dec^{-1} for FeOOH@NiOOH/NF-2, indicating faster reaction kinetics for water oxidation compared to the other samples (Fig. 3b)

The electrochemical double layer capacitance (C_{dl}) values of the as-prepared samples and bare NF electrodes were calculated from cyclic voltammetry (CV) cycles (Fig. S2, Supporting Information). The FeOOH@NiOOH/NF-2 sample exhibited a higher C_{dl} value (2.337 mF cm^{-2}), indicating a larger electrochemical active surface area (Fig. 3c). Additionally, electrochemical impedance spectroscopy (EIS) was employed to evaluate the OER kinetics of the samples, with charge transfer resistance (R_{ct}) calculated from fitting the Nyquist curve with an equivalent-circuit model (Fig. 3d). The charge transfer resistance value of FeOOH@NiOOH/NF-2 was found to be 1.83 Ω, suggesting faster charge transfer at the electrode/electrolyte interface.

The stability of the sample for OER was confirmed through both CV and i-t testing. There was no obvious reduction in overpotential at a current density of 20 mV cm^{-2} observed after 1000–3000 CV cycles (Fig. 3e and Fig. S3, Supporting Information). SEM images revealed that the corrugation nanorod morphology of the FeOOH@NiOOH product sample was still evident on the NF surface after 3000 CV cycles (Fig. S4, Supporting Information). TEM analysis further confirmed the presence of nanosheets on the surface of the nanorods (Fig. S5, Supporting Information). These results demonstrate the stability of the FeOOH@NiOOH/NF-2 sample after 3000 CV cycles. Additionally, the i-t plot indicated almost no decay in current density over a continuous 24-hour period of OER operation (Fig. 3f), suggesting the high stability and durability of our sample.

The HER performance of the commercial 20 % Pt/C sample was evaluated which exhibited the best HER performance, reaching a current density of 10 mA cm^{-2} with only an overpotential of 38 mV in a 1 M KOH solution (Fig. S6a and Table S4, Supporting Information). Among the as-prepared composite samples, the FeOOH@NiOOH/NF-2 sample displayed the best HER performance, with an overpotential of 150 mV at a current density of 10 mA cm^{-2}, demonstrating comparable or superior performance to Fe and Ni-based oxyhydroxide catalysts under similar conditions (Table S5, Supporting Information). The FeOOH/NF and NiOOH/NF samples exhibited poor OER performance with higher overpotential than the other FeOOH@NiOOH/NF-X samples, and the overpotential further increased for the pure NF under the same conditions. This suggests that the enhanced HER performance of the FeOOH@NiOOH/NF-X composites are due to the synergistic effect between the NiOOH nanosheet and FeOOH nanorod. The FeOOH@NiOOH/NF-2 catalyst demonstrated the smallest Tafel slope value, except 20 % Pt/C catalyst (Fig. S6b, Supporting Information), indicating effective reaction kinetics for HER.

The R_{ct} values of the samples increased in the following order: FeOOH@NiOOH/NF-2 < FeOOH@NiOOH/NF-3 < FeOOH@NiOOH/NF-4 < FeOOH@NiOOH/NF-1 < FeOOH/NF-2 < NiOOH/NF-2 < NF-2 (Fig. S6c, Table S4, Supporting Information). The smaller R_{ct} value of 7.9 Ω of FeOOH@NiOOH/NF-2 indicates more efficient charge transfer at the electrode/electrolyte interfaces. FeOOH@NiOOH/NF-2 demonstrates durability for HER activity in alkaline conditions, with almost no change in overpotential observed at a current density of 10 mV cm^{-2} after 1000–3000 CV cycles (Fig. S6d,e, Supporting Information). TEM images after 3000 CV cycles of post-HER clearly show nanosheets observed on the surface of nanorods (Fig. S7, Supporting Information). The XPS analysis of the Ni 2p region of the FeOOH@NiOOH/NF-2 product shows two spin–orbit doublet peaks of Ni $2p_{3/2}$ and Ni $2p_{1/2}$ bands and satellites of Ni $2p_{3/2}$ and Ni $2p_{1/2}$ bands (Fig. S8a, Supporting Information), with almost identical binding energy to that of the fresh sample. No obvious changes in binding energy are observed in the Fe $2p_{3/2}$ and Fe $2p_{1/2}$ bands of the Fe element in the nanocomposite (Fig. S8b, Supporting Information). Almost no current density loss is observed in the i-t plot for continuous 24 h of OER operation (Fig. S6f, Supporting Information). These results indicate that the FeOOH@NiOOH/NF-2 sample is quite stable and durable in alkaline conditions.

After evaluating the excellent OER and HER activity in alkaline conditions of the FeOOH@NiOOH/NF-2 catalyst, the overall water splitting performance was tested. The FeOOH@NiOOH/NF-2 composite was directly used as both the anode and cathode for overall water splitting. The cell voltage of FeOOH@NiOOH/NF-2||FeOOH@NiOOH/NF-2 was measured to be 1.59 V at a current density of 10 mA cm^{-2}, demonstrating almost similar performance to that of the Pt/C||RuO_2 pair electrodes (with a cell voltage of only 1.58 V at a current density of 10 mA cm^{-2}) (Fig. 4**a**). However, the FeOOH@NiOOH/NF-2||FeOOH@NiOOH/NF-2 electrodes reached a high current density of 70 mA cm^{-2}, whereas the Pt/C||RuO_2 pair shows water splitting performance only up to 40 mA cm^{-2} current density. The FeOOH@NiOOH/NF-2||FeOOH@NiOOH/NF-2 configuration displays comparative or superior water splitting performance compared to Pt/C||RuO_2 and reported electrode couples for overall water splitting (Table S6, Supporting Information). Furthermore, the FeOOH@NiOOH/NF-2-2||FeOOH@NiOOH/NF pair shows good durability for at least 100h without any negligible current density loss. These results suggest that the FeOOH@NiOOH/NF-2||FeOOH@NiOOH/NF-2 pair exhibits both good overall water splitting performance and stability.

3.3. Theoretical results

Additionally, a DFT study was undertaken to elucidate and confirm the active site and catalytic mechanism for HER and OER in the experimentally observed heterostructure. Model structures of pristine NiOOH, FeOOH, and FeOOH@NiOOH heterostructure are presented in Fig. S9 (Supporting Information). Comparative analysis of the 2D plot of electrostatic potential revealed that pristine NiOOH has a higher work function of 6.94 eV, while pure FeOOH has a lower work function of 5.55 eV (Fig. 5**a**). Within the heterojunction, the work function was optimized to 6.20 eV, which may contribute to superior performance compared to individual NiOOH and FeOOH. This optimized work function may also indicate enhanced charge transfer capacity, beneficial for the OER process, and increased stability of the resulting heterojunction. The electron localization function (ELF) maps of NiOOH, FeOOH, and NiOOH@FeOOH heterojunction (Fig. 5b) demonstrate the highest electronic cloud density in the heterojunction, particularly at the interface where Ni and Fe atoms are connected. The higher ELF of Fe compared to Ni suggests charge accumulation at the Fe sites. Calculations of net charges for Fe and Ni atoms further support a strong electronic modulation effect in the heterostructure, with Fe exhibiting

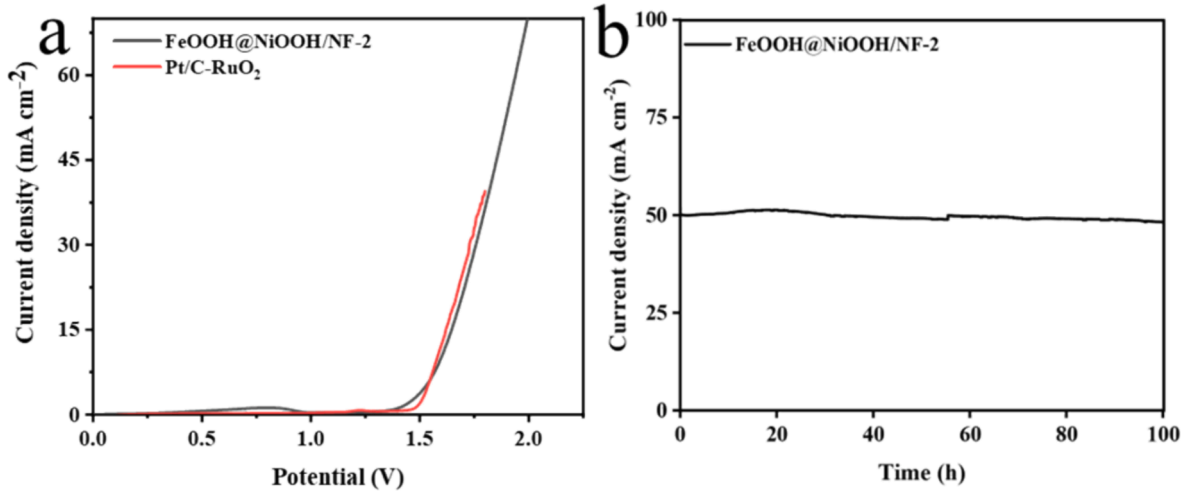

Fig. 4. A) polarization curve of FeOOH@NiOOH/NF-2||FeOOH@NiOOH/NF-2 and Pt/C||RuO_2 electrodes for water electrolysis in 1 M KOH with a scanning rate of 5 mV/s. b) The amperometric (i-t) curve of FeOOH@NiOOH/NF-2 catalyst for long run stability.

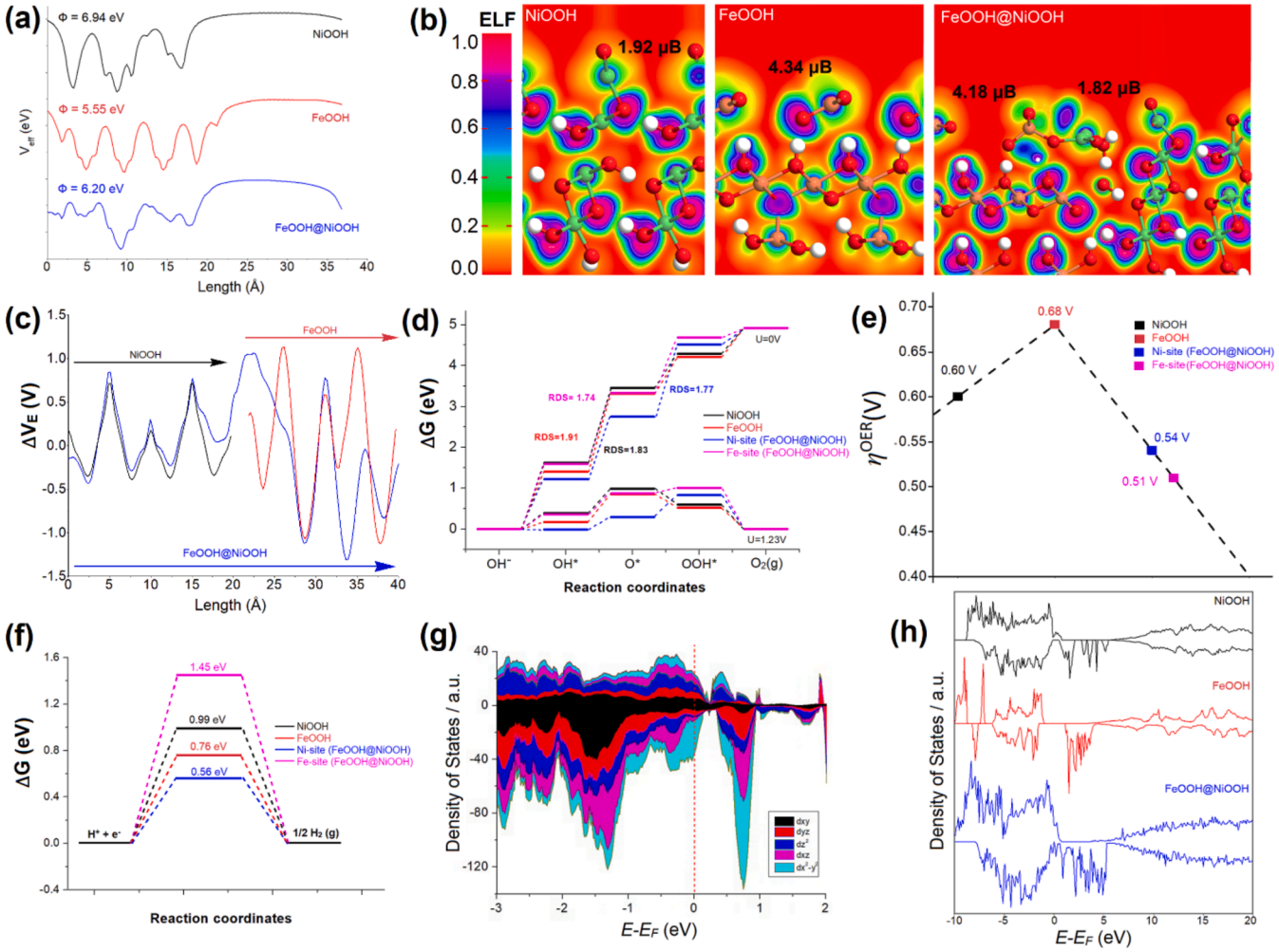

Fig. 5. (a) 2D plot of the effective potential, (b) ELF, and (c) comparative 2D plot of electrostatic difference potential of NiOOH(100), FeOOH(100), and FeOOH@NiOOH (100). (d) Calculated free energy diagram of the OER process on the surface of NiOOH, FeOOH, and FeOOH@NiOOH-2 at U = 0 and U = 1.23 V. (e) OER overpotential, (f) calculated free energy diagram of HER process, (g) DOS of the five Fe 3d orbitals in FeOOH@NiOOH, (h) Comparative DOS of NiOOH, FeOOH, and FeOOH@NiOOH.

higher interaction energy for water molecule. The simulated magnetic moments of Ni in NiOOH and Fe in FeOOH are 1.92 and 4.34 μB, respectively. In the heterojunction, these values decrease to 1.82 and 4.18 μB, indicating a change in the spin state of Fe from high-spin to low-spin. We suggest that this change may improves catalytic activity, contributing to higher OER/HER performance in the FeOOH@NiOOH heterojunction compared to pure NiOOH and FeOOH. The 2D electrostatic difference potential (Fig. 5c) demonstrates FeOOH site within the FeOOH@NiOOH heterojunction is became more negative compared to pristine FeOOH. This synergistic effect in the heterojunction, leading to enhanced charge separation and reduced energy barriers for the reaction. So, charge transformation occurred between NiOOH and FeOOH within the heterojunction and may responsible for efficient OER performance. The oscillations in the electrostatic difference potential of FeOOH@NiOOH indicate a greater ability to separate charges, potentially lowering energy barriers for the OER/HER and improving overall catalytic activity compared to pristine materials

The mechanism of NiOOH, FeOOH, and FeOOH@NiOOH at U = 0 and U = 1.23 V (Fig. 5d), and optimized OER intermediates adsorbed on slab models (Fig. S10, Supporting Information) were employed to analyze the OER kinetics. At U = 0, *O formation is identified as the rate-determining step for NiOOH and the Fe site of the FeOOH@NiOOH heterojunction, while *OOH intermediate formation is the rate-determining step for the Ni site of FeOOH@NiOOH. The free energy diagrams at U = 0 suggest that the Fe site of FeOOH@NiOOH has the lowest rate-determining step compared to other species. A similar trend is observed at U = 1.23 V. Therefore, the Fe site of the FeOOH@NiOOH heterostructure demonstrates superior OER catalytic performance, aligning with our experimental results. So, the formation of FeOOH@-NiOOH promotes charge accumulation on the Fe sites, facilitating intermediate adsorption and enhancing OER activity. In contrast, FeOOH exhibits a large rate-determining step of 1.91 eV, indicating poor OER performance. However, in the FeOOH@NiOOH heterostructure, charge accumulation at Fe sites reduces the rate-determining step to 1.74 eV, improving overall OER performance. Calculate OER overpotentials of NiOOH and FeOOH samples are 0.60 V and 0.68 V, respectively, while 0.54 V for the Ni site and 0.51 V for the Fe site in FeOOH@NiOOH heterojunction catalysts (Fig. 5e). The theoretical simulations highlight the FeOOH@NiOOH heterostructure's outstanding OER activity, attributing it to lower energy barriers that enhance electron transfer between the Fe and Ni centres.

Besides OER calculations, identical models were applied for HER simulations, involving the adsorption of a hydrogen atom on the catalysts' active sites. We are aware that NiOOH, FeOOH, and their heterojunction are excellent catalysts for the OER. However, our consideration is that if one site of the heterojunction is proven to be active for OER, it is reasonable to anticipate that the remaining site might be proficient for the HER. The Gibbs free energy for HER was determined (Fig. 5f) and indicate that the Ni site of FeOOH@NiOOH exhibits the lowest ΔG_H at 0.56 eV, while the ΔG_H values for NiOOH is 0.99 eV, and Fe site of FeOOH and FeOOH@NiOOH are 0.76 eV and 1.45 eV, respectively. This reveals that the Fe site in the heterojunction performs poorly in HER, whereas it excels in OER.

Further insights are gained from the density of states (DOS) of the five 3d orbitals of Fe in FeOOH@NiOOH as shown in Fig. 5g. In Fig. 5g, the increased electron density of Fe in the d^2_{xy} orbital (spin down) leads to a reduction in the magnetic moment (4.18 μB). Theoretical calculations suggest that the Fe spin state (magnetic moment) in the FeOOH@NiOOH heterojunction is manipulated by the neighboring Ni through the 3d electrons. This also suggests that charge transformation occurred between Ni and Fe atoms. Analyzing the comparative total DOS of NiOOH, FeOOH, and FeOOH@NiOOH heterojunction (Fig. 5h), it is evident that the DOS near the Fermi level (spin down) is significantly enhanced in the heterojunction. Fe atoms in the heterojunction make a substantial contribution to the DOS near the Fermi level, thereby modulating the electronic structure and creating a greater number of active electrons for the OER.

All these results show that in FeOOH@NiOOH heterojunction Fe sites displays best OER performance and Ni identified as the optimal active site for HER. Thus, alterations in the electron structure of the heterojunction, changes in the magnetic moment of active sites, increased electron density of Fe in the d^2_{xy} orbital, and a high DOS near the Fermi level, responsible for the lower overpotential of OER and HER which leading to enhance water splitting performance.

4. Conclusion

In summary, FeOOH@NiOOH catalysts on NF were synthesized at very low temperature as a high active electrocatalyst for overall water splitting. The formed corrugation structure and time-dependent optimized FeOOH@NiOOH/NF-2 sample exhibited bifunctional electrocatalyst with excellent OER and HER performance, and good stability and durability in alkaline solution. Water splitting device of FeOOH@NiOOH/NF-2 electrodes display voltages of 1.59 at current densities of 10 mA cm^{-2}. Furthermore, DFT study comprehensively explores the FeOOH@NiOOH heterojunction's catalytic behavior, unravelling key insights into its electronic structure, magnetic moments, and charge transfer capabilities. The observed improvements in OER and HER performance, attributed to altered electronic states and enhanced charge separation at the heterojunction interface, underscore the potential of this material for advanced electrocatalytic applications.

CRediT authorship contribution statement

Sun Hua: Conceptualization, Data curation, Formal analysis, Writing – original draft. **Sayyar Ali Shah:** Funding acquisition, Project administration, Software, Validation, Writing – review & editing. **Gabriel Engonga Obiang Nsang:** Data curation, Investigation. **Rani Sayyar:** Data curation, Formal analysis, Investigation. **Badshah Ullah:** Data curation, Formal analysis. **Noor Ullah:** Data curation, Formal analysis. **Naseem Khan:** Data curation, Formal analysis. **Aihua Yuan:** Conceptualization, Funding acquisition, Project administration, Writing – review & editing. **Abd. Rashid bin Mohd Yusoff:** Validation, Writing – review & editing. **Habib Ullah:** Conceptualization, Methodology, Project administration, Software, Supervision, Writing – original draft, Writing – review & editing.

Declaration of competing interest

The authors declare that they have no known competing financial interests or personal relationships that could have appeared to influence the work reported in this paper.

Data availability

Data will be made available on request.

Acknowledgments

We are thankful to the National Natural Science Foundation of China (under research grant no. 22150410332) and the start-up foundation for the introduction of talent at Jiangsu University of Science and Technology, China. The authors would like to acknowledge the use of the University of Exeter's Advanced Research Computing facilities in carrying out this work. For the purpose of open access, the author has applied a Creative Commons Attribution (CC BY) license to any Author Accepted Manuscript version arising.

Appendix A. Supplementary data

Supplementary data to this article can be found online at https://doi.org/10.1016/j.jcis.2024.09.219.

References

[1] Y.J. Li, Y.J. Sun, Y.N. Qin, W.Y. Zhang, L. Wang, M.C. Luo, H. Yang, S.J. Guo, Recent Advances on Water-Splitting Electrocatalysis Mediated by Noble-Metal-Based Nanostructured Materials, Adv. Energy Mater. 10 (2020) 1903120.

[2] S. Paygozar, A.S.R. Aghdam, E. Hassanizadeh, R. Andaveh, G.B. Darband, Recent progress in non-noble metal-based electrocatalysts for urea-assisted electrochemical hydrogen production, Int. J. Hydrogen Energy 48 (2023) 7219–7259.

[3] H.N. Sun, X.M. Xu, Y.F. Song, W. Zhou, Z.P. Shao, Designing High-Valence Metal Sites for Electrochemical Water Splitting, Adv. Funct. Mater. 31 (2021) 2009779.

[4] M.M. Cai, X.Y. Lu, Z.H. Zou, K.L. Guo, P.X. Xi, C.L. Xu, The Energy Level Regulation of CoMo Carbonate Hydroxide for the Enhanced Oxygen Evolution Reaction Activity, ACS Sustain. Chem. Eng. 7 (2019) 6161–6169.

[5] F. Guo, T.J. Macdonald, A.J. Sobrido, L. Liu, J. Feng, G. He, Recent Advances in Ultralow-Pt-Loading Electrocatalysts for the Efficient Hydrogen Evolution, Adv. Sci. 10 (2023) 2301098.

[6] Z.S. Lu, H. Yang, G.C. Qi, Q. Liu, L.G. Feng, H. Zhang, J. Luo, X.J. Liu, Efficient and Stable pH-Universal Water Electrolysis Catalyzed by N-Doped Hollow Carbon Confined RuIrOx Nanocrystals, Small (2023), 2308841.

[7] L.A. She, G.Q. Zhao, T.Y. Ma, J. Chen, W.P. Sun, H.G. Pan, On the Durability of Iridium-Based Electrocatalysts toward the Oxygen Evolution Reaction under Acid Environment, Adv. Funct. Mater. 32 (2022) 2108465.

[8] W.Z. Huang, J.T. Li, X.B. Liao, R.H. Lu, C.H. Ling, X. Liu, J.S. Meng, L.B. Qu, M. T. Lin, X.F. Hong, X.B. Zhou, S.L. Liu, Y. Zhao, L. Zhou, L.Q. Mai, Ligand Modulation of Active Sites to Promote Electrocatalytic Oxygen Evolution, Adv. Mater. 34 (2022) 2200270.

[9] D. Liu, H.Q. Ai, J.L. Li, M.L. Fang, M.P. Chen, D. Liu, X.Y. Du, P.F. Zhou, F.F. Li, K. H. Lo, Y.X. Tang, S. Chen, L. Wang, G.C. Xing, H. Pan, Surface Reconstruction and Phase Transition on Vanadium-Cobalt-Iron Trimetal Nitrides to Form Active Oxyhydroxide for Enhanced Electrocatalytic Water Oxidation, Adv. Energy Mater. 10 (2020) 2002464.

[10] L. Wang, Y. Wen, Y. Ji, H. Cao, S. Li, S. He, H. Bai, G. Liu, L. Zhang, H. Bao, J. Wang, Y. Li, B. Zhang, H. Peng, The 3d–5d orbital repulsion of transition metals in oxyhydroxide catalysts facilitates water oxidation, J. Mater. Chem. A 7 (2019) 14455–14461.

[11] J. Lee, D. Seo, S. Won, T.D. Chung, Understanding the role of nickel-iron (oxy) hydroxide (NiFeOOH) electrocatalysts on hematite photoanodes, Sustainable, Energy Fuel 5 (2021) 501–508.

[12] A. Taniguchi, K. Ishii, T.K.N. Nguyen, T. Uchikoshi, Y. Kubota, N. Matsushita, Y. Suzuki, Two-step electrochemical deposition of Ni(OH)2/FeOOH bilayer electrocatalyst for oxygen evolution reaction, Mater. Lett. 317 (2022) 132118.

[13] C.Y. Sun, Q.T. Song, J.L. Lei, D. Li, L.J. Li, F.S. Pan, Corrosion of Iron-Nickel Foam to In Situ Fabricate Amorphous FeNi (Oxy)hydroxide Nanosheets as Highly Efficient Electrocatalysts for Oxygen Evolution Reaction, ACS Appl. Energy Mater. 4 (2021) 8791–8800.

[14] F. Nur Indah Sari, S. Abdillah, J.-M. Ting, FeOOH-containing hydrated layered iron vanadate electrocatalyst for superior oxygen evolution reaction and efficient water splitting, Chem. Eng. J. 416 (2021) 129165.

[15] Y. Hao, Y. Li, J. Wu, L. Meng, J. Wang, C. Jia, T. Liu, X. Yang, Z.-P. Liu, M. Gong, Recognition of Surface Oxygen Intermediates on NiFe Oxyhydroxide Oxygen-Evolving Catalysts by Homogeneous Oxidation Reactivity, J. Am. Chem. Soc. 143 (2021) 1493–1502.

[16] H. Xu, Y. Hu, X. Lin, D. Liu, J. Liang, X. Bian, K. Madhav Reddy, H.-J. Qiu, Single-crystal nanoporous high-entropy (oxy)hydroxides nanosheets for electrocatalysis: Structure and electronic dual enhancement, Appl. Surf. Sci. 633 (2023) 157624.

[17] Y.F. Liu, W.G. Li, Y.H. Ma, D.L. Fan, Core-Shell Dendritic Superstructural Catalysts by Design for Highly Efficient and Stable Electrochemical Oxygen Evolution Reaction, Adv. Mater. Interfaces 7 (2020) 2000777.

[18] J.N. Hausmann, R. Beltrán-Suito, S. Mebs, V. Hlukhyy, T.F. Fässler, H. Dau, M. Driess, P.W. Menezes, Evolving Highly Active Oxidic Iron(III) Phase from Corrosion of Intermetallic Iron Silicide to Master Efficient Electrocatalytic Water Oxidation and Selective Oxygenation of 5-Hydroxymethylfurfural, Adv. Mater. 33 (2021) 2008823.

[19] B. Wu, S. Gong, Y. Lin, T. Li, A. Chen, M. Zhao, Q. Zhang, L. Chen, A Unique NiOOH@FeOOH Heteroarchitecture for Enhanced Oxygen Evolution in Saline Water, (2022) 2108619.

[20] Z. Wan, H. Yu, Q. He, Y. Hu, P. Yan, X. Shao, T.T. Isimjan, B. Zhang, X. Yang, In-situ growth and electronic structure modulation of urchin-like Ni–Fe oxyhydroxide on nickel foam as robust bifunctional catalysts for overall water splitting, Int. J. Hydrogen Energy 45 (2020) 22427–22436.

[21] K. Wang, H.F. Du, S. He, L. Liu, K. Yang, J.M. Sun, Y.H. Liu, Z.Z. Du, L.H. Xie, W. Ai, W. Huang, Kinetically Controlled, Scalable Synthesis of γ-FeOOH Nanosheet Arrays on Nickel Foam toward Efficient Oxygen Evolution: The Key Role of In-Situ-Generated γ-NiOOH, Adv. Mater. 33 (2021) 2005587.

[22] D.R. Chowdhury, L. Spiccia, S.S. Amritphale, A. Paul, A. Singh, A robust iron oxyhydroxide water oxidation catalyst operating under near neutral and alkaline conditions, J. Mater. Chem. A 4 (2016) 3655–3660.

[23] W. Wu, L. Peng, B. Min, J. Huang, S. Liu, K. Lu, S. Lu, D. Jing, M. Zheng, M. Liu, Activated overall water splitting over a Ni-Fe layered double hydroxide electrocatalyst by V doping and sulfuration, Appl. Energy Combust. Sci. 14 (2023) 100148.

[24] Y. Zhou, Z. Wang, Z. Pan, L. Liu, J. Xi, X. Luo, Y. Shen, Exceptional Performance of Hierarchical Ni-Fe (hydr)oxide@NiCu Electrocatalysts for Water Splitting, Adv. Mater. 31 (2019) 1806769.

[25] X. Zhang, H. Zhong, Q. Zhang, Q. Zhang, C. Wu, J. Yu, Y. Ma, H. An, H. Wang, Y. Zou, C. Diao, J. Chen, Z.G. Yu, S. Xi, X. Wang, J. Xue, High-spin Co3+ in cobalt oxyhydroxide for efficient water oxidation, Nat. Commun. 15 (2024) 1383.

[26] C.J. An, Novel Interconnected Nickel-Iron Layered Double Hydroxide Nanoweb Structure for High-Performance Supercapacitor Electrodes, Adv. Mater. Interfaces 10 (2022) 2201993.

[27] L. Yang, Z. Liu, S. Zhu, L. Feng, W. Xing, Ni-based layered double hydroxide catalysts for oxygen evolution reaction, Mater. Today Phys. 16 (2021) 100292.

[28] A.S. Batchellor, S.W. Boettcher, Pulse-Electrodeposited Ni–Fe (Oxy)hydroxide Oxygen Evolution Electrocatalysts with High Geometric and Intrinsic Activities at Large Mass Loadings, ACS Catal. 5 (2015) 6680–6689.

[29] M. Liu, J. Wang, H. Wu, S. Li, Y. Shi, N. Cai, Construction of an electrode with hierarchical three-dimensional NiFe-oxyhydroxides by two-step electrodeposition for large-current oxygen evolution reaction, Int. J. Hydrogen Energy 51 (2024) 626–637.

[30] F. Meng, S.A. Morin, S. Jin, Rational solution growth of α-FeOOH nanowires driven by screw dislocations and their conversion to α-Fe_2O_3 nanowires, J. Am. Chem. Soc. 133 (2011) 8408–8411.

[31] H. Xiao, H. Shin, W.A. Goddard III, Synergy between Fe and Ni in the optimal performance of (Ni, Fe) OOH catalysts for the oxygen evolution reaction, Proc. Natl. Acad. Sci. 115 (2018) 5872–5877.

[32] M. Amini, Y. Mousazade, Z. Zand, M. Bagherzadeh, M.M. Najafpour, Ultra-small and highly dispersive iron oxide hydroxide as an efficient catalyst for oxidation reactions: a Swiss-army-knife catalyst, Sci. Rep. 11 (2021) 6642.

[33] M. Ristić, S. Musić, M. Godec, Properties of γ-FeOOH, α-FeOOH and α-Fe_2O_3 particles precipitated by hydrolysis of Fe^{3+} ions in perchlorate containing aqueous solutions, J. Alloy. Compd. 417 (2006) 292–299.

[34] M. Nishi, Y. Kuwayama, J. Tsuchiya, T. Tsuchiya, The pyrite-type high-pressure form of FeOOH, Nature 547 (2017) 205–208.

[35] A.J. Mackay, Society, β-ferric oxyhydroxide—Akaganeite, Mineral. Mag. 33 (1962) 270–280.

[36] S. Shanmugapriya, S. Surendran, D.J. Moon, J.Y. Kim, H. Lee, S.C. Jesudass, K. Veeramani, S. Mahadik, G. Janani, H. Choi, I.G. Kim, P. Jung, J. Heo, K. Hong, Y. I. Park, U. Sim, Ni(OH)2NiOOH 2D-nanosheets tailored with FeOOH nanorods: A synergy of morphological engineering towards bifunctional overall water splitting, Int. J. Hydrogen Energy 54 (2024) 1552–1562.

[37] L. Bai, S. Lee, X. Hu, Spectroscopic and electrokinetic evidence for a bifunctional mechanism of the oxygen evolution reaction, Angew. Chem. Int. Ed. 60 (2021) 3095–3103.

[38] Y. Li, J. Huang, X. Hu, L. Bi, P. Cai, J. Jia, G. Chai, S. Wei, L. Dai, Z. Wen, Fe Vacancies Induced Surface FeO_6 in Nanoarchitectures of N-Doped Graphene Protected β-FeOOH: Effective Active Sites for pH-Universal Electrocatalytic Oxygen Reduction, Adv. Funct. Mater. 28 (2018) 1803330.

[39] G. Zhang, Q. Qin, W. Luo, Y. Liu, C. Jin, J. Hao, J. Zhang, W. Zheng, A combination–decomposition method to synthesize two-dimensional metal sulfide–amine hybrid nanosheets: a highly efficient Fe-based water oxidation electrocatalyst, Chem. Commun. 54 (2018) 4617–4620.

[40] J. Chen, F. Zheng, S.-J. Zhang, A. Fisher, Y. Zhou, Z. Wang, Y. Li, B.-B. Xu, J.-T. Li, S.-G. Sun, Interfacial interaction between FeOOH and Ni–Fe LDH to modulate the local electronic structure for enhanced OER electrocatalysis, ACS Catal. 8 (2018) 11342–11351.